Chapter 5

3D-ROTATIONAL X-RAY IMAGING

Advances in Interventional Volume Imaging

Volker Rasche[1], Michael Grass[2], Robert Manzke[3]
[1]University Hospital Ulm, Ulm, Germany; [2]Philips Research, Hamburg, Germany; [3]Philips Research, Briarcliff Manor, NY, USA

Abstract: 3D-rotational X-ray imaging is a rather new volume imaging technique on conventional C-arm X-ray systems. This contribution covers the basics of the underlying mathematics of three-dimensional X-ray imaging, the data acquisition protocols, and calibration and reconstruction techniques. Furthermore, an overview of the current clinical application of 3D-rotational X-ray imaging is presented.

Keywords: 3D-rotational angiography, C-arm calibration, cone beam reconstruction

1. INTRODUCTION

Three-dimensional rotational X-ray imaging (3D-RX) is a rather new imaging method based on the rotational angiography (RA) technique, which was introduced in the early 90s. RA is an extension of the conventional angiography technique, in which the gantry of an X-ray system is rotated around the patient while acquiring X-ray projections during continuous contrast agent (CA) injection. Initially, the main application of RA was in the field of interventional neuroradiology[1,2]. Compared to conventional angiography the improved visualization of vascular anatomy by the multiple angles of view available from the rotational acquisition results in superior information on complex 3D vascular structures. This additional anatomic information significantly improved e.g. the angiographic assessment of aneurysms making it an excellent adjunct in e.g. the investigation of subarachnoid hemorrhage. In the following years RA has been introduced to various other fields including assessment of the renal arteries[3,4] and

G. Spekowius and T. Wendler (Eds.), Advances in Healthcare Technology, 65-80.

visualization of the coronary artery tree, in which a significant reduction of overall X-ray and contrast agent dose could be realized[5].

Based on the RA protocols, the projection data acquired during a RA run have been utilized for volume reconstruction, resulting in the so-called 3D rotational angiography (3D-RA) technique. Since then, the application of volume reconstruction has become more and more standard in interventional neuroradiology e.g. for improved assessment of the shape and size of aneurysms[6], the planning of radiation treatment of arterialvenous malformations (AVM)[7], or just to get more insights in the vascular structure[8]. With increasing availability, other applications such as the renal arteries[9] and peripheral angiography[10] have been added.

Up to now, the application of 3D-RA has been limited to high-contrast objects such as selectively enhanced vascular trees. With the advent of new X-ray systems providing significantly improved characteristics for volume reconstruction, the application of 3D-RA to more general volume X-ray imaging (3D-RX) is on its verge.

This contribution covers the basic mathematics of three-dimensional X-ray imaging, the basics of acquisition, calibration and reconstruction on current X-ray systems and gives an overview on clinical application of 3D-RX.

1.1 Mathematical description of the 3D reconstruction from X-ray projections

1.1.1 The Radon transformation

The Radon transformation R of a three-dimensional object function $f(x,y,z) = f(\vec{x})$ is defined as the complete set of integrals over planes E through the object. With

$$E : \vec{x} \cdot \vec{\xi} = \rho \qquad \vec{x} = \begin{pmatrix} x \\ y \\ z \end{pmatrix} \qquad \vec{\xi} = \begin{pmatrix} \sin\theta\cos\lambda \\ \sin\theta\sin\lambda \\ \cos\theta \end{pmatrix}$$

the Radon transform $Rf(\rho,\lambda,\theta) = Rf(\rho\vec{\xi})$ at a specific distance ρ to the origin with orientation $\vec{\xi}$ (Figure 5-1) can be calculated according to

$$Rf\left(\rho\vec{\xi}\right) = \int_{-\infty}^{+\infty}\int_{-\infty}^{+\infty}\int_{-\infty}^{+\infty} f(\vec{x})\,\delta\left(\vec{x}\cdot\vec{\xi} - \rho\right)d\vec{x}\,, \qquad [1]$$

which can be reformulated as

$$Rf(\rho\vec{\xi}) = \int_{-\infty}^{+\infty}\int_{-\infty}^{+\infty} f(\rho\vec{\xi},s,t)dsdt, \qquad [2]$$

with $\rho\vec{\xi}$ defining the orientation and position of the plane and s and t being two variables running along two orthogonal axes in the plane.

A complete Radon transformation of an object function $f(\vec{x})$ requires the calculation of all Radon values $Rf(\rho\vec{\xi})$ with $\rho\in$ [-∞,∞], $\lambda\in$ [-π/2,π/2) and $\theta\in$ [0,2π).

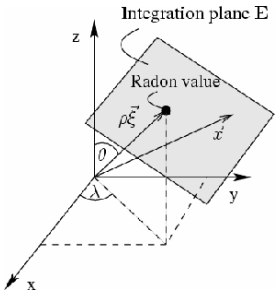

Figure 5-1. A single Radon value is obtained by integration of the object function over a specific plane, defined according to its location and orientation in space.

1.1.2 The X-ray projection

In the ideal basic X-ray imaging experiment (Figure 5-2), the subject of investigation *f(x,y,z)* is irradiated by an X-ray beam along a line *L*, along which an intensity I_0 is emitted from the X-ray tube towards the detector element. While the X-ray beam is passing through the subject, its intensity is attenuated according to the tissue-specific attenuation factor *f(x,y,z)*. Finally, the intensity I_{out} of the attenuated X-ray beam is measured by means of an X-ray detector. For simplicity, in the following description of the mathematics, the attenuation coefficients are assumed to be independent on the energy of the X-ray photons and no non-ideal effects such as scatter are considered.

According to the law of Lambert-Beer, the attenuated intensity of the X-ray beam I_{out} can be calculated as

$$I_{out} = I_0 e^{-\int_L f(x,y,z)dl}. \qquad [3]$$

Equation [3] can be easily reformulated to the so-called line integral value p, the value of which is independent on the initial intensity I_0 and hence only depending on the tissue attenuation properties

$$p = \ln \frac{I_{out}}{I_0} = -\int_L f(x,y,z)dl \,. \qquad [4]$$

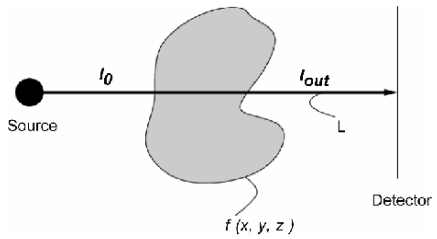

Figure 5-2. The basic X-ray imaging experiment.

As shown in Figure 5-3, with $\vec{T}$ being the position of the focal spot, each line on the detector belongs to a certain plane $E(\rho\vec{\xi})$ through the object and the projection value $p(\vec{T},s,t)$ can be rewritten as $Xf(\rho\vec{\xi}, \kappa)$ with κ being the angle between the central beam and the specific X-ray beam along the s-direction. With r being the distance along the ray, $Xf(\rho\vec{\xi}, \kappa)$ can be calculated according to

$$Xf(\rho\vec{\xi},\kappa) = \int_{-\infty}^{+\infty} f(\rho\vec{\xi},r,\kappa)dr \qquad [5]$$

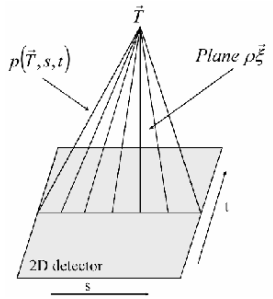

Figure 5-3. Relation between a single projection value and the corresponding Radon plane.

1.1.3 Relation between the X-ray projection and the Radon transformation

The calculation of the integral of a certain plane $E(\rho\vec{\xi})$ involves the integration of $Xf(\rho\vec{\xi},\kappa)$ along the line on the detector, which results to

$$\int_{-\frac{\pi}{2}}^{+\frac{\pi}{2}} Xf(\rho\vec{\xi},\kappa)d\kappa = \int_{-\frac{\pi}{2}}^{+\frac{\pi}{2}}\int_{-\infty}^{+\infty} f(\rho\vec{\xi},r,\kappa)drd\kappa\,. \qquad [6]$$

Transformation of equation [2] into the X-ray coordinate systems yields

$$Rf(\rho\vec{\xi}) = \int_{-\frac{\pi}{2}}^{+\frac{\pi}{2}}\int_{-\infty}^{+\infty} f(\rho\vec{\xi},r,\kappa)rdrd\kappa, \qquad [7]$$

which differs from equation [6] by the proportional factor r and hence the Radon transform values can not directly be obtained by integration along lines on the detector. In 1991 Grangeat[11] presented a mathematical framework, which relates the X-ray values to the 1st derivative of the Radon transform

$$\frac{\partial}{\partial\rho}Rf\left(\rho\vec{\xi}\right) = \frac{1}{\cos^2\beta}\frac{\partial}{\partial s}\int_{-\infty}^{+\infty}\frac{\overline{SO}}{\overline{SA}}Xf\left(s\left(\rho\vec{\xi}\right),t\right)dt. \qquad [8]$$

Here, SO defines the source detector distance, SA the distance between the source and the respective detector element (s,t) and β defines the angle between the central beam and the detector t-value. This mathematical framework enables the calculation of Radon transform values from X-ray projection data.

1.1.4 Radon inversion formula

An inversion formula to reconstruct an object function from its Radon transform data was introduced by Natterer[12] in 1986

$$f(\vec{x}) = -\frac{1}{8\pi^2}\int_{-\frac{\pi}{2}}^{+\frac{\pi}{2}}\int_{0}^{2\pi}\frac{\partial^2}{\partial\rho^2}Rf\left(\left(\rho\vec{\xi}\right)\cdot\vec{\xi}\right)\sin\theta\, d\lambda\, d\theta. \qquad [9]$$

This formula represents the basis for all exact reconstruction algorithms based on Radon inversion.

1.1.5 Data sufficiency criteria

During a real imaging experiment, data are acquired while moving the X-ray tube and detector around the patient. To ensure complete filling of Radon space, for each plane with normal $\rho\vec{\xi}$ at least one source point position, which belongs to that plane, must be available. Tuy[13] and Smith[14] formulated the so-called sufficiency condition as:

If on every plane that intersects the object, there exists at least one cone beam source point, then one can reconstruct the object.

1.2 3D-RX

The 3D-RX imaging method is directly based on the 3D Rotational Angiography (3D-RA) data acquisition protocol[14]. The underlying projection data is acquired on conventional C-arm systems. During continuous projection data acquisition, the C-arm gantry is rotated around the object under investigation by at least 180°. To get to the final volume information, the projection data has to be calibrated and reconstructed.

The different steps involved are elucidated in the following subsections.

1.2.1 Data acquisition

A schematic view of the projection data acquisition procedure is presented in Figure 5-4 for the example of an Angiography acquisition. Projection data are normally acquired along a planar trajectory by rotating the C-arm gantry around the patient either in head or lateral position. Depending on the anatomy, a caudal or cranial tilt of the gantry of up to 30° is used during data acquisition. The target area is positioned in the center-of-rotation (iso-center). Depending on the application, projection images are taken at a frame rate between 12.5 and 60 fr/s and the rotation speed of the system may be up to 55°/s. Valid combinations of frame rate and rotation speed are defined by the number of projections required for a certain application and a clinically acceptable maximal acquisition time. For high-

contrast applications such as conventional three-dimensional rotational angiography applications, in which a reconstruction of a contrast-agent enhanced vascular tree is obtained, typically 100 projections are taken within 4s over an angular range of 220°. In case of more soft-tissue contrast applications such as brain imaging to check for intracerebral bleedings, up to 750 projections are being used acquired within 25s.

1.2.2 Calibration

Due to the open design of conventional X-ray C-arm systems, during rotation of the gantry, the relative position of the tube to the detector is changing due to slight bending and vibration of the gantry and, in case of image intensifier based systems, distortions to the projections are introduced by earth magnetic field interactions and vignetting. For 3D reconstruction, however, the knowledge of the accurate position of the tube and the detector and distortion-free projections are mandatory to avoid image quality degradation. The measurement of the real projection geometry and the projection image distortions is one of the most important steps in 3D-RX.

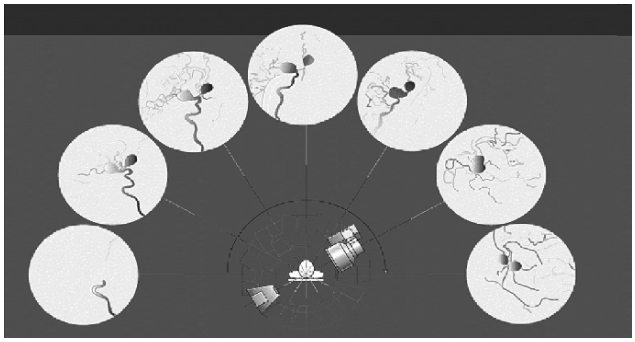

Figure 5-4. Example of a 3D-RX data acquisition for 3D rotational angiography.

A variety of calibration approaches have been introduced[16-19]. Among these, the utilization of dedicated geometrical phantoms with known markers represents a very stable approach to achieve calibration results of high accuracy. For each trajectory used, the calibration and projection parameters are measured once during the installation of the system and normally remain constant over months due to the excellent reproducibility of the systems.

The calibration procedure is separated into the acquisition of projection data of two phantoms, used for the measurement of the image distortions and focal spot position, and the projection geometry.

The first phantom consists of two parallel grid plates (Figure 5-5) manufactured in glass fiber. Grid 1 for the II-distortion measurement consists of equally spaced grid-points (e.g. 1.5 mm bronze beads; grid-distance equal to15 mm). Grid 2 for the focal spot measurements consists of grid-points (e.g. 2 mm bronze beads) arranged on a circle equally spaced at 7.5°. Both test grids are coupled by rods and mounted in front of the detector housing.

The second phantom (Figure 5-5) used for measurement of the projection direction consists of 20 beads, positioned in the corners of a regular polyeder (dodecaeder). Three additional markers are placed on the z-axis of the geometry phantom.

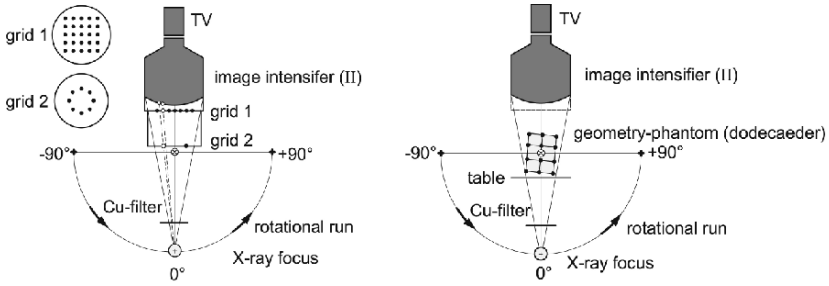

Figure 5-5. Principle of the two-step calibration approach.

1.2.2.1 Measurement of the image distortion

The projected beads of the grid are automatically determined in each projection image and the functional relation between the imaged grid points and the real grid points is determined by modeling the distortions along the x-axis and the y-axis by bivariate polynoms[20] independently for each projection view. Once the distortion coefficients are known, each projection image is warped by means of bilinear interpolation before reconstruction.

1.2.2.2 Focal spot determination

The automatically recognized points of grid 2 are matched to a circle in a least-square-fit. From the diameter of the determined circle and its location relative to the detector, the position of the focus spot is estimated independently for each view. A typical measurement of the focal spot position is shown in Figure 5-6 for a half circular trajectory. The average error in the determined focal spot position is in the order of 0.1mm.

1.2.2.3 Geometrical projection parameter determination

After automatic extraction of the projected beads, a comparison between the forward projected position of the known phantom beads with known projection orientation and the real projection of the phantom is used for determination of the projection direction. For performing a sufficient least squares error fit, all 23 beads of the object are considered during the optimization. A typical outcome of the measurement of the projection geometry is shown in Figure 5-6.

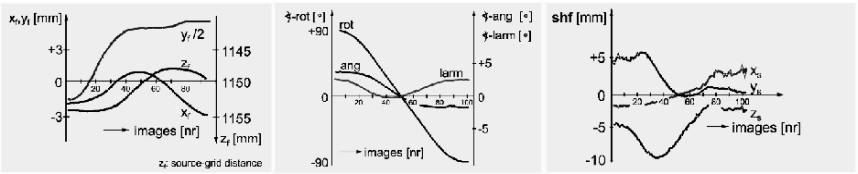

Figure 5-6. Typical values for the tube position (left), projection orientation (middle) and the iso-center measurement (right) for a 180° trajectory.

1.2.3 Reconstruction

After distortion correction, the knowledge of the accurate projection geometry is used to apply a 3D cone-beam reconstruction from the projection data. It can be shown that the inverse Radon transformation results into a simple three-dimensional convolution back projection in case the projection data are acquired on a circular trajectory. This so-called Feldkamp reconstruction technique was introduced in 1984 by Feldkamp, Davis, and Kress[21]. The original Feldkamp algorithm is described by:

$$f(x,y,z)=\frac{1}{2}\int_0^{2\pi}\left(\frac{D}{d}\right)^2\left[\left(p(s,t,\phi)\cos\gamma\right)*h(s)\right]d\phi\,. \qquad [10]$$

Here, (s,t,ϕ) describes the detector element at (s,t) acquired with angle ϕ of the circular trajectory, γ is the angle between the vector from the source to the center of the detector and the vector from the source to the detector element (s,t), $h(s)$ describes the convolution kernel, D is the distance from the origin to the position of the source and d is the length of the vector from the source to the voxel under consideration projected onto the central ray. $h(s)$ is chosen as a pure band-limited ramp filter tangential to the ideal source-detector trajectory as

$$h(s) = \frac{1}{2}\sin c(s) - \frac{1}{4}\sin c^2\left(\frac{s}{2}\right) . \qquad [11]$$

In equation [10] a perfectly circular trajectory with equiangular spacing of the source position along the trajectory is assumed. These conditions are not met for a typical 3D-RX acquisition. In order to compensate for the deviations from the ideal trajectory, three modifications to the original Feldkamp algorithm must be applied[22]:

- Consideration of the true detector and source position as measured during the calibration process. Since the deviations from a planar circular trajectory are usually small, a modification of the filter direction is not required. It is kept parallel to the projection of the source trajectory onto the detector.
- Compensation for an uneven sampling density along the circular trajectory, caused by the acceleration and the deceleration of the gantry during the rotational acquisition. This is achieved by calculating the sample distance of projection measurements along the source trajectory. Each projection measurement represents a certain part of the acquisition path and its relation to the complete path length yields the corresponding weight.
- Finally, for acquisition paths, which represent a circular arc with more than a half circle plus the fan angle, a Parker weighting is applied in order to compensate for rays measured redundantly[23].

1.2.4 System performance

Due to certain system limitations such as the improperly filled Radon space caused by the circular trajectory, the limited dynamic range, spatial extent and speed of the current detectors, and limited suppression of scatter, the volume imaging performance in 3D-RX does not yet meet the standards of CT. However, analysis of the imaging performance reveals[24,25] that the small pixel size of the X-ray detectors down to $165^2 um^2$ enables volume imaging at unique isotropic spatial resolution of up to 30lp/cm in all spatial directions. Furthermore, utilizing the high dynamic range of up to 14Bit in case of the recent flat panel detectors enables significantly improved contrast resolution below 30 Hounsfield units[25] (Figure 5-7).

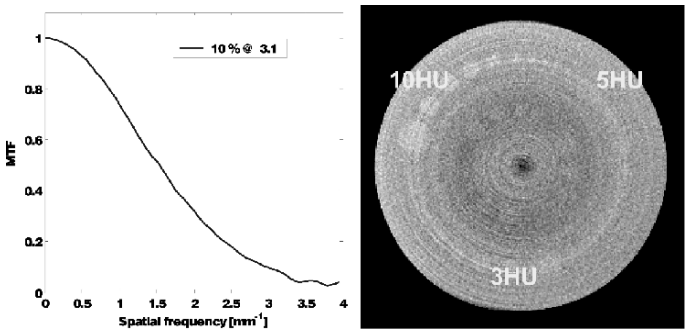

Figure 5-7. Modulation transfer function (left) and contrast-resolution (right) of 3D-RX performed on a Philips Allura FD10 X-ray system. The curve on the left shows the average MTF of all spatial dimensions. The image on the right shows an image of the soft-tissue section (CTP515 of the Catphan 500, The Phantom Laboratory, Cambridge, USA). Data courtesy of Dr. Georg Rose, Philips Research Aachen.

1.3 Future directions

Future directions in 3D-RX are aiming for providing CT-like image quality on interventional C-arm systems. Major targets are the improved compensation for projection truncations[26] and the complete filling of Radon space by using dedicated trajectories, which perform rotations around more than a single axis[27]. Further work focuses on the reduction of the impact of scatter[28].

Furthermore, so-called hybrid systems combining some CT components such as closed gantry concepts with X-ray components such as real two-dimensional detectors are currently entering clinical evaluation[29].

2. CLIINICAL EXAMPLES

In the following, some examples of the use of 3D-RX in the current clinical environment are given. The current application can roughly be categorized into high-contrast applications, in which the contrast between the object and the background is typically in the order of several hundred HU, and medium- to soft-tissue contrast applications, in which the contrast difference may go down close to 20 HU. For all applications, currently circular trajectories covering an angular range of about 220° are utilized. Major differences results from the number of projections utilized for the projections and the exposure settings. For high contrast objects, typically less projections and higher kV settings are used.

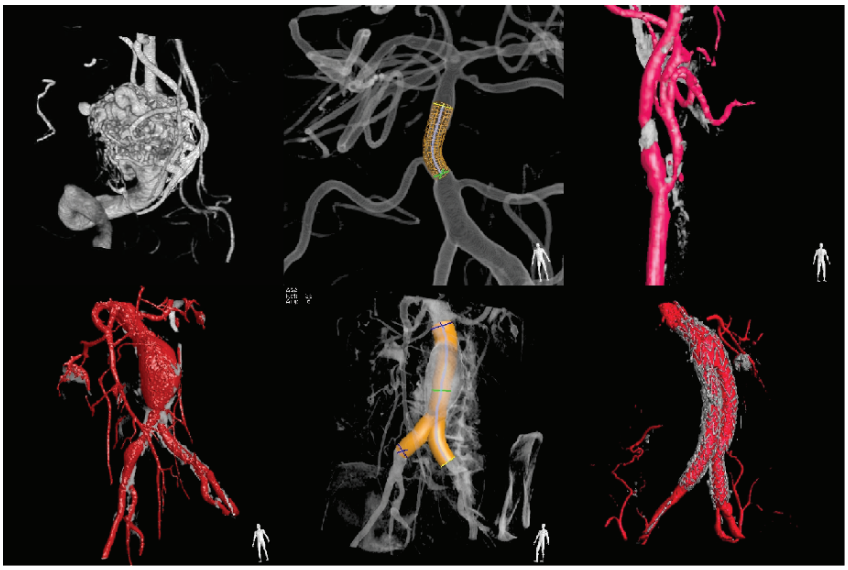

Figure 5-8. Examples of typical vascular application of 3D-RX. Examples show reconstruction of an AVM (upper left), stent planning for intracerebral stenting (upper middle), carotid stenosis with calcified plaque (upper right), abdominal aortic aneurysm (AAA) with calcified plaque (lower left), stent planning for AAA (lower middle) and stent visualization after deployment (lower right).

2.1 High contrast applications

The use of 3D-RX for providing high-quality three-dimensional angiograms is still the paramount clinical application. Here, a typical high-contrast protocol is applied since the vascular structures are selectively enhanced by direct injection of the contrast media into the vascular structure under investigation. Most applications are in the field of interventional neuroradiology for improved assessment of three-dimensional vessel structures and quantitative assessment of vascular and aneurysm properties. Furthermore, due to the intrinsic high contrast of calcium, the angiographic information can be augmented by superposition of the calcified structures. With deeper clinical penetration of the techniques, application in the fields of abdominal aortic aneurysm as well as for other abdominal and peripheral arterial structures have become more common. Some typical examples of the usage of 3D-RX in the vascular field are shown in Figure 5-8.

Besides the angiographic application, the application of 3D-RX for bone imaging in the field of surgery and orthopedics is getting more and more attention. Here the projection data is normally obtained on mobile surgery

C-arm systems[30,31] with motorized propeller rotation. Main anatomical targets are the head, spine, joints and extremities. Figure 5-9 and 5-10 show the application of 3D-RX on a surgical system for providing anatomic information prior to ear-nose-throat (ENT) surgery and for guiding a cochlea implant implantation procedure.

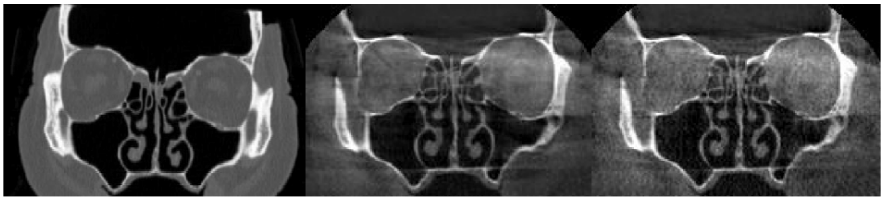

Figure 5-9. Comparing of conventional CT to of an intact post mortem head to 3D-RX on a mobile surgery X-ray system (upper row). From left to right a CT, 3D-RX high quality (375 projections) and a 3D-RX normal quality (151 projections). Data courtesy of Prof. Dr. med. et Dr. med. dent. Beat Hammer, Cranio-Faciales-Centrum, Hirslanden Clinic, Aarau, Switzerland.

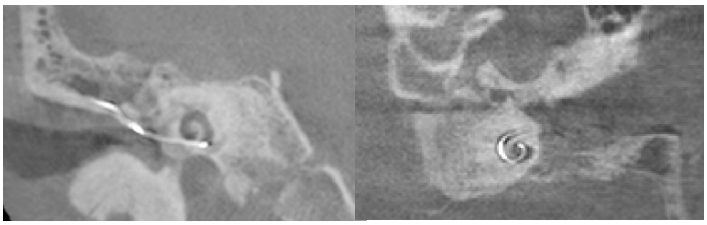

Figure 5-10. Example of the intra-surgical use of 3D-RX during the implantation of a cochlea implant. (Data courtesy of Dr. B. Carelsen, AMC, Amsterdam, The Netherlands).

2.2 Medium- to soft-tissue contrast applications

With the introduction of the new flat panel detectors providing up to 14 bits of dynamic range, the application of 3D-RX in the field of medium- to soft-tissue contrast resolution is approached. Recent studies proved the applicability of 3D-RX for the assessment of e.g. fresh intra-cerebral bleedings as depicted in Figure 5-11.

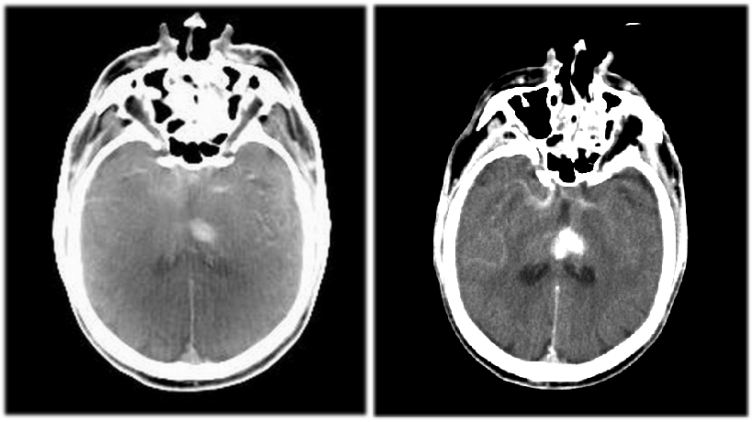

Figure 5-11. Comparison 3D-RX (left) with CT (right) for imaging of fresh intra-cerebral bleeding. (Data courtesy of Prof. Moret, Foundation Ophthalmologique de Rothshild, Paris, France).

3. DISCUSSION

In conclusion, three-dimensional imaging on X-ray systems (3D-RX) has dramatically progressed over the last years. The application of 3D-RX in the field of interventional neuroradiology has entered clinical routine. New application of 3D-RX, especially in the field of surgery and orthopedics, are on the horizon and initial clinical evaluations show promising results. The extension of 3D-RX to other fields demanding medium- to soft-tissue contrast is a continuous process, which will likely be accelerated by the introduction of new X-ray systems.

From the current perspective, 3D-RX will remain in the realm of interventional imaging providing three-dimensional information during interventional procedures without the need for additional imaging equipment such as MRI or CT.

The major advantage of 3D-RX results from the huge two-dimensional detectors, which enable full organ coverage during a single rotation at very high spatial resolution. Whether that will motivate its application to diagnostic imaging may be questioned, especially since the ever increasing number of detector elements in CT systems will get close to the X-ray detectors.

REFERENCES

1. M. Schumacher, K. Kutluk, D. Ott, Digital rotational radiography in neuroradiology, *AJNR Am J Neuroradiol* **10**(3), 644-649 (1989).
2. D.J. Hoff, M.C. Wallace, K.G. ter Brugge, F. Gentili, Rotational angiography assessment of cerebral aneurysms, *AJNR Am J Neuroradiol* **15**(10), 1945-1948 (1994).
3. H.M. Klein, D. Vorwerk, J. Neuerburg, R.W. Gunther, Rotational angiography of the renal arteries, *Rofo* **162**(3), 249-251(1995).
4. H.R. Seymour, M.B. Matson, A.M. Belli, R. Morgan, J. Kyriou, U. Patel, Rotational digital subtraction angiography of the renal arteries: technique and evaluation in the study of native and transplant renal arteries, *Br J Radiol* **74**(878), 134-141 (2001).
5. J.T. Maddux, O. Wink, J.C. Messenger, B.M. Groves, R. Liao, J. Strzelczyk, S.Y. Chen, J.D. Carroll., Randomized study of the safety and clinical utility of rotational angiography versus standard angiography in the diagnosis of coronary artery disease, *Catheter Cardiovasc Interv* **62**(2), 167-174 (2004).
6. T. Hirai, Y. Korogi, K. Suginohara, K. Ono, T. Nishi, S. Uemura, M. Yamura, Y. Yamashita, Clinical usefulness of unsubtracted 3D digital angiography compared with rotational digital angiography in the pretreatment evaluation of intracranial aneurysms, *AJNR Am J Neuroradiol* **24**(6), 1067-1074 (2003).
7. F. Colombo, C. Cavedon, P. Francescon, L. Casentini, U. Fornezza, L. Castellan, F. Causin, S. Perini. Three-dimensional angiography for radiosurgical treatment planning for arteriovenous malformations, *J Neurosurg* **98**(3), 536-543 (2003).
8. R. Anxionnat, S. Bracard, J. Macho, E. Da Costa, R. Vaillant, L. Launay, Y. Trousset, R. Romeas, L. Picard, 3D angiography. Clinical interest. First applications in interventional neuroradiology, *J Neuroradiol* **25**(4), 251-262 (1998).
9. G. Hagen, J. Wadstrom, L.G. Eriksson, P. Magnusson, M. Magnusson, A. Magnusson, 3D rotational angiography of transplanted renal arteries: influence of an extended angle of rotation on beam-hardening artifacts, *Acta Radiol* **46**(2), 170-176 (2005).
10. J.C. van den Berg, F.L. Moll, Three-dimensional rotational angiography in peripheral endovascular interventions, *J Endovasc Ther* **10**(3), 595-600 (2003).
11. P. Grangeat, Mathematical framework of cone–beam 3D reconstruction via the first derivative of the radon transform In: G.T. Herman, A.K. Louis, F. Natterer (eds.), *Mathematical Methods in Tomography, Lecture Notes in Mathematics*, 66-97 (Springer, Berlin, 1991).
12. F. Natterer, *The Mathematics of Computerized Tomography*, ISBN 0-471-90959-9 (John Wiley and Sons, New York 1986).
13. H.K. Tuy, An Inversion Formula for Cone-Beam Reconstruction, *SIAM J Appl Math* **43**(3), 546-552 (1983).
14. B.D. Smith, Image reconstruction from cone-beam projections. *IEEE Trans Med Img* **4**(1), 14–25 (1985).
15. R. Kemkers, J. Op de Beek, H. Aerts, R. Koppe, E. Klotz, M. Grass, J. Moret, 3D Rotational Angiography: First Clinical application with use of a standard Philips C-arm system, *Proc Computer Assisted Radiology, 13th International Congress and Exhibition, Tokyo, 182-187 (1998)*.
16. A. Rougee, C. Picard, C. Ponchut, Y. Trousset, Geometrical calibration for 3D X-ray imaging, *Proc SPIE Medical Imaging*, *Image Capture, Formatting, and Display* Vol.**1897**, 161-169 (1993).
17. R. Koppe, E. Klotz, J. Op de Beek, H. Aerts, 3D vessel reconstruction based on Rotational Angiography, *Proc Computer Assisted Radiology, 9th International Congress and Exhibition, Berlin, 101-107* (1995).

18. R. Koppe, E. Klotz, J. Op de Beek, H. Aerts, Digital stereotaxy/stereotactic procedures with C-arm based Rotation-Angiography, *Proc Computer Assisted Radiology, 10th International Congress and Exhibition, Paris, 17-22 (1996)*.
19. R. Fahrig, M. Moreau, D.W. Holdsworth, Three-dimensional computed tomography reconstruction using a C-arm mounted XRII: Correction of image intensifier distortion, *Med Phys* **24**(7), 1097-1106 (1997).
20. P. Haaker, E. Klotz, R. Koppe, R. Linde, Real-time distortion correction of digital X-ray II/TV-systems*, Int Journal of Card Imaging* **6**, 39-45 (1990/91).
21. L.A. Feldkamp, L.C. Davis, J.W. Kress, Practical Cone-Beam Algorithms, *J Opt Soc Am* **6**, 612-619 (1984).
22. M. Grass, R. Koppe, E. Klotz, R. Proksa, M.H. Kuhn, H. Aerts, J. Op de Beek, R. Kemkers, Three-dimensional reconstruction of high contrast objects using C-arm image intensifier projection data, *Comp Med Imag Graph* **23**, 311-321 (1999).
23. D.L. Parker, Optimal short scan convolution reconstruction for fanbeam CT, *Medical Physics* **9**(2), 254 – 257 (1982).
24. V. Rasche, C. Graeff, M. Grass, T. Istel, E. Klotz, R. Koppe, G. Rose, H. Schomberg, B. Schreiber, Performance of image intensifier equipped X-Ray systems in three dimensional imaging, *Proc Computer Assisted Radiology, 10th International Congress and Exhibition, London,* 187-192 (2003).
25. V. Rasche, B. Schreiber, J.N. Noordhoek, P. van de Haar, D. Schaefer, J. Wiegert, Comparison of Flat Panel Detectors and Image Intensifiers for Volume Imaging on Interventional C-Arc Systems, *RSNA, 83rd Scientific Session* (2003).
26. H. Schomberg, Image Reconstruction from Truncated Cone-Beam Projections, *Proc 2004 IEEE International Symposium on Biomedical Imaging: From Macro to Nano*, 575-578 (2004).
27. H. Schomberg, Complete Source Trajectories for C-Arm Systems and a Method for Coping with Truncated Cone-Beam Projections, *Proc 6th International Meeting on Fully 3D Image Reconstruction in Radiology and Nuclear Medicine*, 221-224 (2001).
28. J. Wiegert, M. Bertram, D. Schaefer, N. Conrads, J. Timmer, T. Aach, G. Rose, Performance of standard fluoroscopy antiscatter grids in flat-detector-based cone-beam CT, *Proc SPIE Medical Imaging, Physics of Medical Imaging*, Vol. **5368**, 67-78 (2004).
29. J. Lisauskas, M. Ferencik, F. Moselewski, S. Houser, R. Gupta, R. Chan, Morphologic Measurements of ex-Vivo Coronary Arteries from High-Resolution Volume CT, *RSNA* (2004).
30. T. van Walsum, E.B. van de Kraats , B. Carelsen, S.N. Boon, N.J. Noordhoek, W.J. Niessen, Accuracy of Navigation on 3DRX Data Acquired with a Mobile Propeller C-Arm, *Proc 4th Annual Meeting of Computer Assisted Orthopedic Surgery,* 22-23 (2004).
31. B. Carelsen, N.H. Bakker, S.N. Boon, W.J. Fokkens, N.J.M. Freeling, N.J. Noordhoek, Mobile 3D rotational X-ray: comparison with CT in sinus surgery, *Medica Mundi* **48(**3), 4-10 (2004).